ACS Sustainable Chemistry & Engineering

Research Article

pubs.acs.org/journal/ascecg

Facile Surface Modification of Ubiquitous Stainless Steel Led to Competent Electrocatalysts for Overall Water Splitting

Xuan Liu, Bo You, and Yujie Sun*

Department of Chemistry and Biochemistry, Utah State University, Logan, Utah 84322, United States

Ⓢ *Supporting Information*

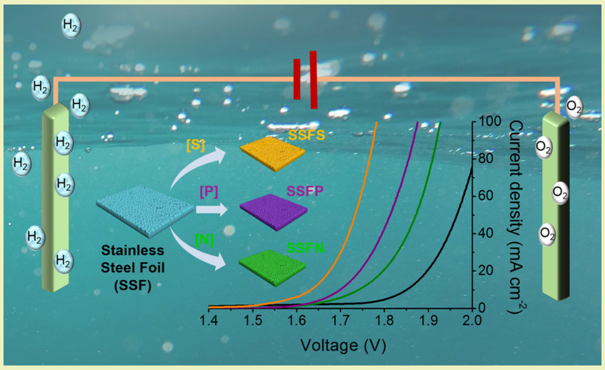

ABSTRACT: Competent and low-cost electrocatalysts play a crucial role in the wide deployment of electrocatalytic water splitting for clean H_2 production. Herein, for the first time, we report that readily available stainless steel can be transformed to competent electrocatalysts for both H_2 and O_2 evolution reactions (HER and OER, respectively) after facile surface modification. Specifically, our sulfurized stainless steel foil (SSFS) could achieve a catalytic current density of 10 mA cm^{-2} at overpotentials of 136 and 262 mV for HER and OER, respectively, in 1.0 M KOH. When SSFS served as the electrocatalysts for both the cathode and the anode, an overall water splitting current density of 10 mA cm^{-2} was obtained at 1.64 V with robust durability. Such a superior performance can rival those of many recently reported water splitting catalysts that consist of expensive elements, contain high-cost supports, or require sophisticated synthesis. In addition, excellent water splitting activity was also achieved by SSFS in neutral media, largely expanding its working conditions. Finally, we further demonstrated that analogous phosphorization and nitridation treatments also could substantially enhance the electrocatalytic performance of stainless steel for water splitting, suggesting the great versatility of our surface modification strategy.

KEYWORDS: *Water splitting, Stainless steel, Surface modification, Electrocatalysis*

■ INTRODUCTION

Renewable energy-driven water splitting to produce clean H_2 has been regarded as a promising strategy for meeting the increasing global energy demand and mitigating the environmental impact of the utilization of fossil resources, which are finite and thus unsustainable.[1,2] The sluggish kinetics of both H_2 and O_2 evolution reactions (HER and OER, respectively) of water splitting necessitates the development of competent catalysts.[3,4] Even though Pt-, Ir-, and Ru-based catalysts have long been known to be active for HER and OER, the challenges to their widespread application are their high cost and limited abundance in the Earth's crust. Recent years have witnessed the emergence of a variety of HER and OER catalysts solely composed of earth abundant elements,[5] such as transition metal oxides,[6−9] chalcogenides,[10−19] and pnictides.[20−26] Nevertheless, most water splitting electrocatalysts still require either sophisticated synthesis or expensive reagents and/or supports. To be applicable for large-scale deployment, it is highly desirable to develop a low-cost strategy for catalyst production, preferably based on widely available materials on an industrial scale. In this regard, stainless steel appears to be an attractive catalyst candidate. Commercial stainless steel consists of a large percentage of Fe and Ni, whose oxides and (oxy)hydroxides have been reported to have superior OER activity.[27−30] In addition, stainless steel has been utilized as a cathode material in industrial water electrolysis, albeit requiring cocatalysts.

The potential of stainless steel for water splitting has already been reported. It was found that without any treatment, bare stainless steel exhibited rather poor OER performance.[31] However, upon surface oxidation or electrochemical oxidation−reduction corrosion, stainless steel exhibited improved OER performance.[32−39] In contrast, surface modified stainless steel has been rarely studied as a HER catalyst. Schäfer et al. reported that electrooxidation of Ni42 steel showed some HER activity, requiring a high overpotential of 299 mV to produce 10 mA cm^{-2} at pH 14,[40] which was inferior to those of inexpensive metal chalcogenides and pnictides. To the best of our knowledge, stainless steel-based catalysts have not yet been explored as electrocatalysts in a two-electrode configuration for overall water splitting. Considering its extremely low cost, high level of annual production, and promising active components, we seek to develop competent and bifunctional catalysts based on stainless steel for overall water splitting electrolysis.

Herein, we report that facile sulfurization treatment of stainless steel foil will generate a surface layer of sulfides (SSFS) that exhibit excellent electrocatalytic activities for both HER and OER in alkaline media (1.0 M KOH). Our SSFS required overpotentials of only 136 and 262 mV to reach a current

Received: January 17, 2017
Revised: March 18, 2017
Published: April 11, 2017

DOI: 10.1021/acssuschemeng.7b00182
ACS Sustainable Chem. Eng. 2017, 5, 4778−4784

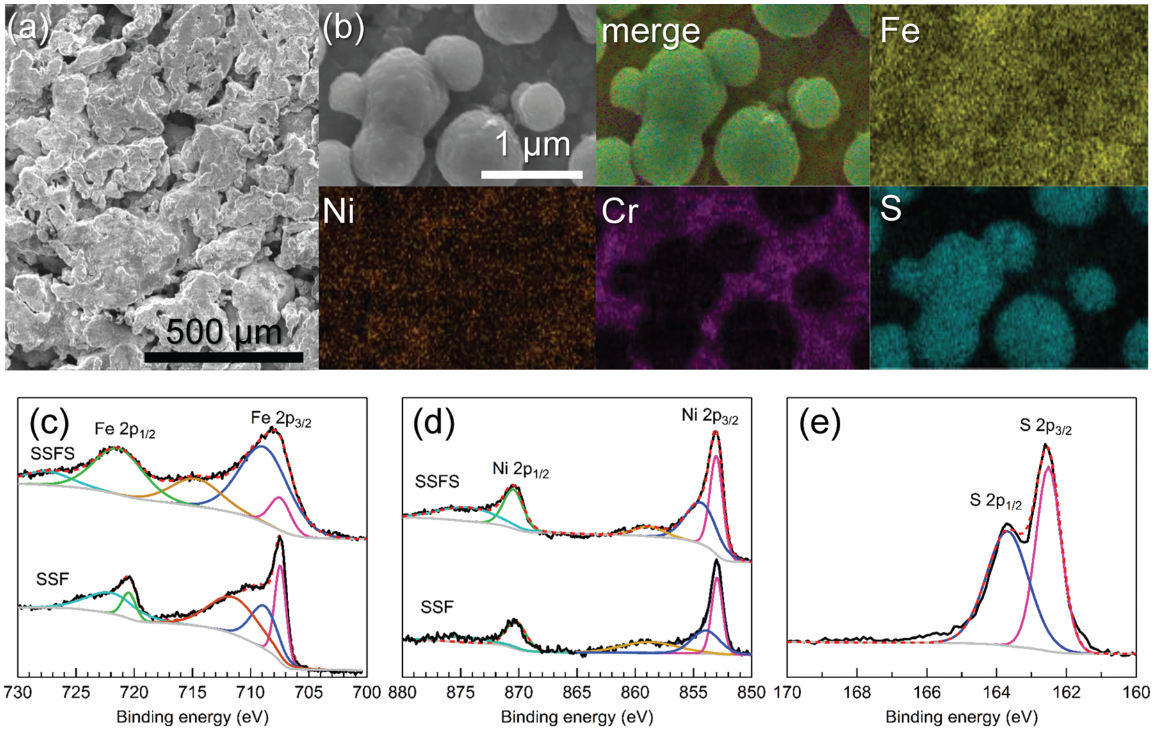

Figure 1. (a) SEM image of SSFS. (b) SEM and corresponding elemental mapping images of SSFS. High-resolution XPS spectra of (c) Fe and (d) Ni of SSF and SSFS, and (e) S of SSFS.

density of 10 mA cm^{-2} for H_2 and O_2 evolution, respectively, significantly better than those of the parent stainless steel foil. When serving as the electrocatalysts for both the cathode and the anode in a two-electrode configuration for overall water splitting, our SSFS catalyst couple reached 10 mA cm^{-2} at 1.64 V, ~220 mV lower than that of the parent stainless steel sample, together with robust stability. SSFS also performed as a competent catalyst for water splitting in a neutral electrolyte. Even more appealing is the fact that such a surface modification strategy can be extended to produce phosphorized and nitridized stainless steel samples, both of which possessed electrocatalytic activities better than those of the untreated samples for water splitting.

EXPERIMENTAL SECTION

Chemicals. Sulfur and sodium hypophosphite monohydrate were purchased from Sigma-Aldrich. Potassium hydroxide and hydrochloride acid were purchased from Fisher. Compressed ammonium gas was purchased from GT&S Inc. All the chemicals were used as received without any further purification. Water was purified with a Barnstead E-Pure system (18 MΩ·cm). Stainless steel foil (SF-316-250-1, MTI Co.) was cut into 0.5 cm × 3 cm pieces, immersed in 20 mL of 5.0 M HCl, and sonicated for 0.5 h. After being thoroughly rinsed with water and ethanol, SSF was stored under vacuum at room temperature.

Preparation of SSFS. A piece of clean SSF was placed at the center of a tube furnace, while 3.0 g of sulfur was placed at an appropriate upstream position. After being flushed with Ar for 20 min, the tube furnace was heated to 400 °C (500 or 600 °C) at a rate of 10 °C min^{-1} and maintained at the end temperature for 1 h. After the furnace had cooled to room temperature, the final sulfurized stainless steel foil (SSFS) was obtained.

Preparation of SSFN and SSFP. The overall synthetic process was very similar to that of SSFS. For the preparation of SSFN, NH_3 was flushed through the tube furnace during the entire annealing process. For the preparation of SSFP, 3.0 g of sodium hypophosphite was used as the phosphorus source. Both samples were heated to the target temperature with the same heating rate and maintained at the target temperature for 1 h.

Characterization. Scanning electron microscopy and elemental mapping analysis were performed on a FEI QUANTA FEG 650 instrument. X-ray diffraction patterns were obtained on a Rigaku MinifexII Desktop X-ray diffractometer. X-ray photoelectron spectroscopy was conducted using a Kratos (Chestnut Ridge, NY) Axis Ultra instrument at the Surface Analysis Laboratory of Nanofab of the University of Utah. The samples were affixed on a stainless steel Kratos sample bar, loaded into the instrument's load lock chamber, and evacuated to 5×10^{-8} Torr before the samples were transferred into the sample analysis chamber under ultra-high-vacuum conditions ($\sim 10^{-10}$ Torr). X-ray photoelectron spectra were recorded using the monochromatic Al Kα source (1486.7 eV) at a 300 μm × 700 μm spot size. Low-resolution survey and high-resolution region scans at the binding energy of interest were collected for each sample. To minimize charging, all samples were flooded with low-energy electrons and ions from the instrument's built-in charge neutralizer. The samples were also sputter-cleaned inside the analysis chamber with 1 keV Ar^+ ions for 30 s to remove adventitious contaminants and surface oxides. X-ray photoelectron spectroscopy (XPS) data were analyzed using CASA XPS software, and energy corrections on high-resolution scans were calibrated by referencing the C 1s peak of adventitious carbon to 284.5 eV.

Electrochemical Measurement. All electrochemical measurements were performed on a Gamry Interface 1000 potentiostat with a three-electrode or two-electrode configuration. SSF (SSFS, SSFN, or SSFP) 0.5 cm × 0.5 cm in size was used as the working electrode, a Ag/AgCl (saturated KCl) electrode as the reference electrode, and a Pt wire as the counter electrode. All the reported potentials for HER and OER were quoted with respect to the reversible hydrogen electrode (RHE) through RHE calibration. For overall water splitting tests, two SSF (SSFS, SSFN, or SSFP) samples were used as both anode and cathode electrodes and the potential scan range was from 1.2 to 2.0 V. *iR* (current times internal resistance) compensation was applied in all the electrochemical experiments to account for the drop in voltage between the reference and working electrodes using Gamry Frame-

DOI: 10.1021/acssuschemeng.7b00182
ACS Sustainable Chem. Eng. 2017, 5, 4778−4784

work Data Acquisition version 6.11. A 20 mL one-chamber electrochemical cell was utilized for overall water splitting electrolysis. The distance between two electrodes was ∼1 cm. The electrolyte (1.0 M KOH) was deaerated with N_2 and stirred at 800 rpm during the whole electrolysis process. The electrochemical impedance spectroscopy measurements were performed with an ac potential amplitude of 30 mV and a frequency range from 1000 kHz to 0.1 Hz.

Quantification of Generated Gases. The generated gases were quantified with a SRI gas chromatography system (model 8610C) equipped with a molecular sieve 13× packed column, a HayesSep D packed column, and a thermal conductivity detector. The oven temperature was maintained at 80 °C, and argon was used as the carrier gas. Controlled potential electrolysis was performed in 1.0 M KOH at 2.4 V for 167 min in an H-type two-compartment cell.

■ RESULTS AND DISCUSSION

SSFS could be prepared in a very straightforward method. A commercially available stainless steel foil was annealed in the presence of sulfur at 400−600 °C for 1 h. Optimization of the annealing temperature demonstrated that 500 °C resulted in the best performance for overall water splitting (Figure S1); therefore, all the following experiments were conducted with SSFS prepared at 500 °C unless noted otherwise.

The scanning electron microscopy (SEM) images of the pristine stainless steel foil (SSF) showed its porous morphology of irregular bricks with a featureless surface (Figure S2). After sulfurization, the resulting SSFS inherited the overall morphology of SSF (Figure 1a). However, close inspection of the high-magnification SEM image (Figure 1b) of SSFS revealed urchinlike microspheres that were drastically different from the relatively smooth surface of SSF (Figure S2b). Elemental mapping images of SSFS (Figure 1b) demonstrated that both Fe and Ni were well distributed throughout the entire foil. It was interesting to find that S was colocalized with those newly formed microspheres, while Cr was almost absent from those microspheres. These elemental mapping results indicated that the newly formed microspheres mainly consisted of iron and nickel sulfides, both of which have been reported to have HER and OER activities.[10−18] A cross sectional SEM image of SSFS (Figure S3) was collected, and the thickness of the surface sulfide layer was roughly 1.9 μm. The corresponding elemental mapping images of the cross section further confirmed the existence of iron and nickel sulfides and the absence of Cr in the sulfide layer. Figure S4 includes the X-ray diffraction (XRD) patterns of SSF and SSFS and compares them with the standard XRD patterns of Fe, $Fe_{1-x}S$, NiS, and $FeNi_2S_4$. The diffraction peaks of SSF at 44.4°, 51.6°, and 75.4° could be assigned to the (111), (200), and (220) facets of stainless steel, respectively.[39] After sulfurization, all of those Fe-based peaks were well-preserved in SSFS, along with small peaks at 33.6°, 48.0°, 56.8°, and 64.6°, which could be attributed to $Fe_{1-x}S$, NiS, and $FeNi_2S_4$, albeit with low resolution. It should be noted that because only the surface of the stainless steel foil was sulfurized while the inner composition of SSFS remained like that of the bulk SSF (Figure S3), the resulting XRD pattern of SSFS should inevitably exhibit the XRD peaks of SSF. It was also apparent that such a mild sulfurization treatment rendered a surface layer of a sulfide mixture with low crystallinity, consistent with reported sulfur-treated steels.[41,42] XPS was further conducted to reveal the composition and valence states of the elements in SSF and SSFS. The XPS survey spectra (Figure S5) of both samples exhibited all the anticipated elements, including Fe, Ni, and Cr, consistent with the SEM elemental mapping results. Figure 1c plots the high-resolution Fe 2p spectra of SSF and SSFS. SSF displayed typical peaks at binding energies of 707.1 eV (metallic Fe) and 709.2 eV (oxidized Fe), while SSFS showed a decreased intensity at 707.1 eV and an increase at 709.2 eV, in agreement with the surface oxidation of Fe during sulfurization.[43,44] The high-resolution Ni $2p_{3/2}$ spectra could be deconvoluted into three subpeaks at binding energies of 852.7, 854.8, and 859.3 eV (Figure 1d), which can be assigned to $Ni^{\delta+}$, oxidized Ni species, and the Ni $2p_{3/2}$ satellite peak, respectively. Similarly, the enhanced intensity of the oxidized Ni species was observed for SSFS relative to SSF. In addition, a well-defined high-resolution S 2p XPS spectrum was obtained for SSFS (Figure 1e), and it could be simulated by two subpeaks at 162.5 and 163.9 eV, corresponding to S $2p_{3/2}$ and $2p_{1/2}$, respectively.

The electrocatalytic OER performance of SSFS together with SSF for comparison was first studied by steady-state linear sweep voltammetry (LSV) in 1.0 M KOH. Figure 2a displays the LSV curves of SSFS for water oxidation in 1.0 M KOH. When the anodic potential was scanned beyond 1.47 V versus the reversible hydrogen electrode (RHE), a rapid increase in current was observed (Figure 2a, inset), accompanied by vigorous O_2 bubble formation on the catalyst surface. However, no catalytic current was observed for SSF until 1.53 V versus the RHE. It should be noted that all the OER LSV curves reported herein were collected from cathodic scans to mitigate the possible interference of catalyst oxidation in the observed catalytic current.[45] In fact, SSFS required overpotentials of only 262, 306, and 370 mV to produce OER current densities of 10, 100, and 1000 mA cm^{-2}, respectively, where the latter two values were approaching those for industrial applications. However, much larger overpotentials were required for SSF to produce current densities of 10 (303 mV) and 100 (361 mV) under the identical condition. The corresponding Tafel plots of SSFS and SSF are included in Figure 2b. Indeed, a smaller Tafel slope (42 mV decade^{-1}) was obtained for SSFS relative to that of SSF (57 mV decade^{-1}), implying the OER kinetics of the former was better. Such a small Tafel slope places SSFS among

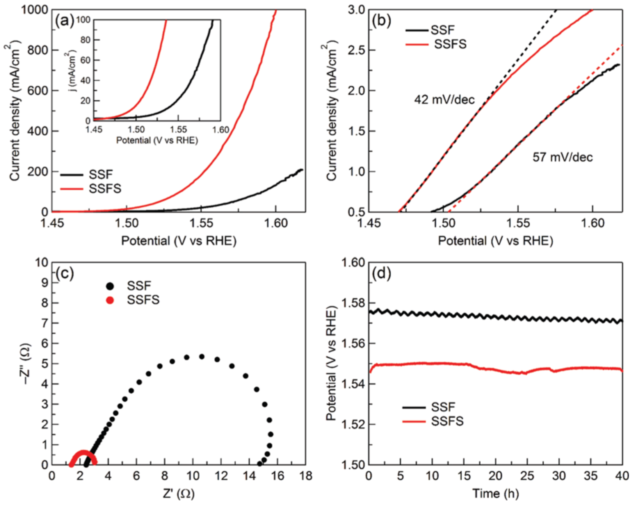

Figure 2. (a) Linear sweep voltammograms of SSF and SSFS for O_2 evolution in 1.0 M KOH at a scan rate of 2 mV s^{-1} (the inset shows the expanded region around the onset of catalysis). (b) Corresponding Tafel plots of SSF and SSFS. (c) Electric impedance spectra of SSF and SSFS measured at 1.523 V vs the RHE. (d) Chronopotentiometric curves of SSF and SSFS at a current density of 50 mA cm^{-2}.

the most active OER electrocatalysts. The better OER kinetics on SSFS was also confirmed by electrochemical impedance spectroscopy (EIS) performed at 1.523 V versus the RHE (Figure 2c). Fitting the EIS spectra of SSFS and SSF according to an equivalent electric circuit (Figure S6) resulted in a charge transfer resistance of 0.00027 Ω for SSFS and 3.43 Ω for SSF (Figure S7), consistent with the enhanced OER performance of the former. Furthermore, the EIS-derived double-layer capacitance (C_c) of SSFS was nearly 9 times that of SSF (Table S1). As double-layer capacitance is widely believed to be proportional to electrochemically active surface area (ECSA) for electrocatalysts with similar compositions,[6−9] a substantially increased ECSA of SSFS was beneficial for its water oxidation electrocatalysis. Besides activity, stability is another crucial factor in assessing an electrocatalyst. Thus, long-term chronoamperometry experiments (40 h) at 50 mA cm^{-2} were conducted with SSFS and SSF (Figure 2d). The required potential was maintained at ∼1.55 V versus the RHE for SSFS over the entire course of electrolysis, while SSF needed a more positive potential (1.575 V vs the RHE) to retain the same current density. Overall, the OER performance of SSFS was comparable or superior to those of many recently reported OER catalysts. For instance, CoFeO$_x$,[46] NiCoO$_x$,[47] and NiFeO$_x$[7] needed overpotentials of 370, 380, and 300 mV, respectively, to reach 10 mA cm^{-2} in 1.0 M KOH. Moreover, our catalyst was among those outstanding stainless steel-based OER electrocatalysts. A detailed comparison between SSFS and representative OER catalysts is given in Table S2. We emphasize that one should be very cautious in comparing the performance of different electrocatalysts with different surface areas, as surface area will strongly impact measured current density.[48]

SSFS after the long-term OER electrolysis described above (denoted as post-OER SSFS) was characterized to investigate its morphology and composition change during electrolysis. The XRD pattern of the post-OER SSFS was very different from that of the fresh SSFS because of the oxidation of sulfide species (Figure S4). The SEM images of the post-OER SSFS demonstrated that it inherited the overall porous morphology while the surface of those microspheres became wrinkled and rougher (Figure S8). The elemental mapping images showed the presence of Fe, Ni, Cr, and S, with a large amount of O (Figure S8). High-resolution XPS spectra of Fe, Ni, and S clearly exhibited increased intensities at binding energies associated with oxidized species (Figure S9). For instance, a prominent peak at 170.2 eV was observed in the S 2p region (Figure S9c), which was attributed to oxidized sulfur moieties (SO$_x$). Elemental analysis of the SSFS after OER determined that the contents of Fe, Cr, Ni, and S in SSFS were 60.8, 17.8, 12.2, and 0.6 mg/100 mg, respectively, while the contents of these elements in as-prepared SSFS were 61.7, 19.4, 12.7, and 1.1 mg/100 mg, respectively (Table S3).

In contrast to a few reports utilizing activated stainless steel as an OER electrocatalyst, the HER activity of stainless steel-based catalysts has rarely been studied. Inspired by those transition metal sulfides (e.g., nickel sulfides) showing promising HER performance,[9−18] we were optimistic that sulfurization would render SSFS active for H_2 evolution, as well. Indeed, quite encouragingly, HER activity was obtained for SSFS in 1.0 M KOH. As shown in Figure 3a, the parent SSF did not exhibit appreciable HER activity, with nearly no catalytic current prior to −0.3 V versus the RHE (Figure 3a, inset). In sharp contrast, a rapid catalytic current of SSFS increased within −0.1 V versus the RHE and rapidly approached 10 and 100 mA cm^{-2} at −0.136 and −0.283 V versus the RHE, respectively, while at these potentials, no catalytic current was obtained from SSF, highlighting the importance of sulfurization. The corresponding Tafel plots (Figure 3b) resulted in very similar Tafel slopes for SSFS and SSF (147−148 mV decade^{-1}), implying that water dissociation likely acted as the rate-limiting step prior to the three fundamental steps (Volmer, Heyrovsky, and Tafel steps) of HER.[47] The improved HER activity of SSFS was further confirmed by the smaller semicircular diameter of its EIS spectrum compared to that of SSF (Figure 3c). Using the same equivalent electric circuit (Figure S6), we derived a double-layer capacitance of SSFS that was nearly 25 times that of SSF (Figure S10 and Table S4), in agreement with a significantly increased ECSA and thus the superior HER performance of the former. The 40 h chronopotentiometry experiments were performed at a current density of −50 mA cm^{-2} for both SSFS and SSF. The stable potential versus time curves shown in Figure 3d demonstrate the robustness of SSFS and SSF for extended H_2 evolution. SSFS required an applied potential nearly 185 mV smaller than that of SSF, as well as 163 mV smaller than that of other reported stainless steel-based catalysts,[39] unambiguously proving the critical role of sulfurization in improving its HER electrocatalytic activity. In fact, the HER performance of SSFS could compete with those of many inexpensive HER catalysts under alkaline conditions (Table S5).

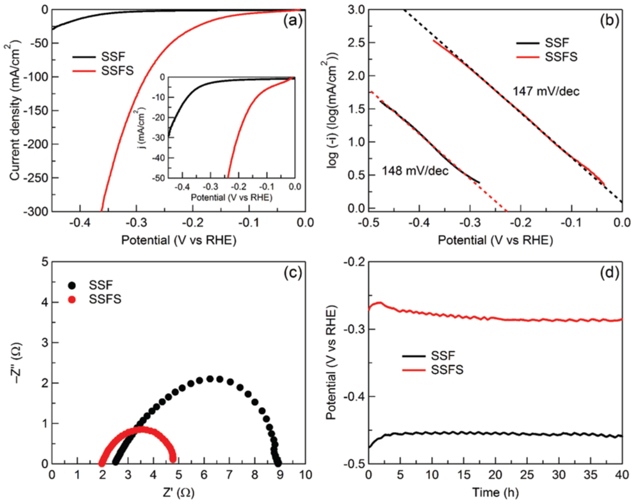

Figure 3. (a) Linear sweep voltammograms of SSF and SSFS for H_2 evolution in 1.0 M KOH at a scan rate of 2 mV s^{-1} (the inset shows the expanded region around the onset of catalysis). (b) Corresponding Tafel plots of SSF and SSFS. (c) Electric impedance spectra of SSF and SSFS measured at −0.327 V vs the RHE. (d) Chronopotentiometric curves of SSF and SSFS at a current density of −50 mA cm^{-2}.

The morphology of the post-HER SSFS was also assessed via SEM. A close inspection of its high-magnification SEM image revealed a rough and fluffy surface that might result from the formation of H_2 bubbles during H_2 evolution (Figure S11). Metal sulfides were still coated on the surface, and no detachment was observed. Elemental mapping images of SSFS after HER demonstrated that Fe, Ni, and S were still well-distributed on the electrode. The XRD pattern proved the presence of the SSFS composition after HER, nearly identical to that of the as-prepared SSFS (Figure S4). Additionally, the high-resolution XPS spectra of Fe, Ni, and S also supported the retention of the original composition, corroborating the superior robustness of SSFS for HER (Figure S12). The more oxidized Ni and Fe species detected via high-resolution XPS spectra could be due to the extended exposure to the aqueous electrolyte (1.0 M KOH) during electrolysis. The contents of Fe, Cr, Ni, and S in SSFS after the long-term HER electrolysis were 61.8, 18.7, 12.3, and 0.9 mg/100 mg, respectively, which were almost identical to those in the as-prepared SSFS, further indicating the excellent stability of SSFS for electrocatalytic H_2 evolution (Table S6).

With the above HER and OER activities of SSFS in hand, it was well anticipated that SSFS could be utilized as both cathode and anode catalysts for overall water splitting. Hence, a two-electrode configuration was adopted to employ SSFS as both the anode and the cathode in 1.0 M KOH. As a comparison, the parent SSF catalyst couple was also included. As shown in Figure 4a, it was apparent that a catalytic current was observed for SSFS when the applied voltage was >1.55 V while SSF needed 1.80 V to produce an appreciable catalytic current (Figure 4a). Remarkably, our SSFS catalyst couple required a voltage of 1.64 V to afford 10 mA cm^{-2}, whereas the SSF counterpart needed an additional 220 mV (1.86 V) to achieve the same current density. Both catalyst couples possessed strong robustness for long-term water electrolysis as shown in Figure 4b, wherein the SSFS catalyst couple saved a voltage of nearly 280 mV compared with the SSF couple in delivering a current density of 50 mA cm^{-2}. The excellent stability of SSFS could also be corroborated by the perfect overlap of the LSV curves before and after the 40 h chronopotentiometry experiment (Figure 4a). Figure 5 plots the produced H_2 and O_2 amounts quantified by gas chromatography and compared them with those values calculated on the basis of the passed charge during electrolysis. The nearly perfect overlap of the experimentally measured and calculated quantities of both gases strongly demonstrated the near unity Faradaic efficiency of our SSFS catalyst couple for overall water splitting.

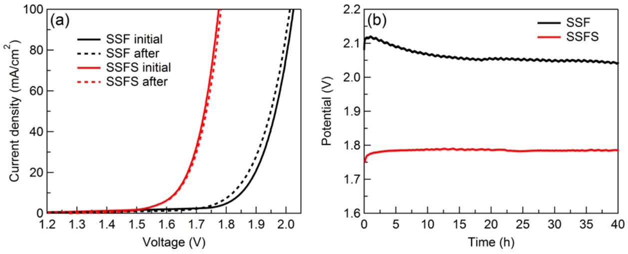

Figure 4. (a) Linear sweep voltammograms of SSF and SSFS that served as both cathode and anode electrocatalysts for overall water splitting at a scan rate of 2 mV s^{-1} in 1.0 M KOH before and after a 40 h electrolysis. (b) Corresponding chronopotentiometric curves of SSF and SSFS catalyst couples for overall water splitting at a current density of 50 mA cm^{-2}.

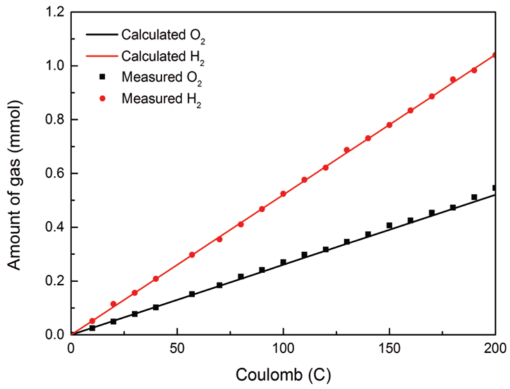

Figure 5. Quantities of gas chromatography-measured gases and theoretically calculated gases for overall water splitting by the SSFS couple in 1.0 M KOH.

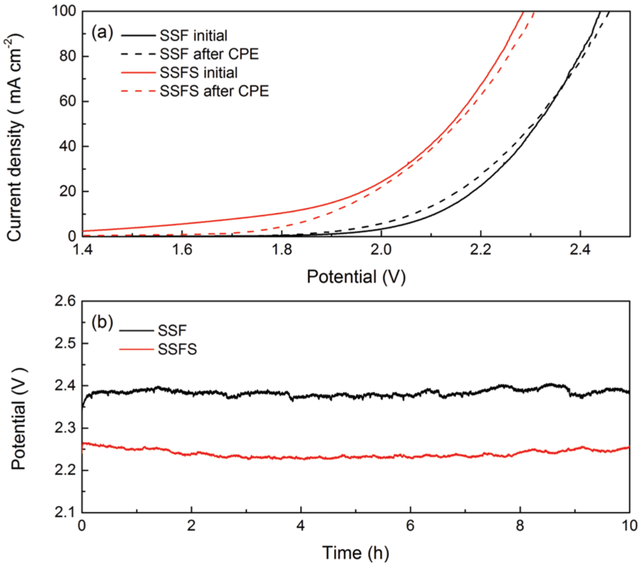

Figure 6. (a) Polarization (scan rate of 2 mV s^{-1}) and (b) chronoamperometry curves (at 50 mA cm^{-2}) of SSFS and SSF for overall water splitting in 1.0 M phosphate buffer (pH 7).

In addition to strong alkaline conditions, water-splitting catalysts that are equally active in neutral media are also very attractive, as they can be integrated with biological systems to yield value-added products[49,50] and/or utilized for seawater splitting with renewable energy sources. Hence, the water splitting performance of SSFS was evaluated in phosphate buffer at pH 7. Figure 6a shows the LSV curves of SSFS for overall water splitting in a two-electrode configuration before and after a 10 h chronoamperometry experiment at 50 mA cm^{-2} (Figure 6b). It was clear that SSFS possessed activity that was greatly enhanced versus that of SSF under neutral conditions, reaching 10 mA cm^{-2} at 1.85 V together with strong robustness.

Encouraged by the aforementioned exciting water splitting performance of SSFS and also inspired by the reported HER and OER activities of transition metal pnictides, we intended to assess the versatility of our surface modification strategy.[51] It was anticipated that stainless steel after nitridation (SSFN) and phosphorization (SSFP) would also exhibit improved water splitting performance. Indeed, after optimization on the annealing temperature, it was found that the best catalytic performance was realized for SSFN and SSFP prepared at 400 and 500 °C, respectively (Figures S13 and S14). SEM images and XRD patterns of SSFN and SSFP are included in Figures S15−S17, showing morphologies and crystallinities similar to those of SSFS. Their XPS spectra also clearly demonstrated the formation of SSFN and SSFP (Figure S18). The LSV curves of SSFN and SSFP for H_2 evolution are compared with those of SSF and SSFS in Figure 7a, while their corresponding OER polarization curves are plotted in Figure 7b. It was apparent that both SSFN and SSFP possessed improved HER and OER activities relative to that of the parent SSF, albeit they are less active than SSFS. The polarization curves of overall water

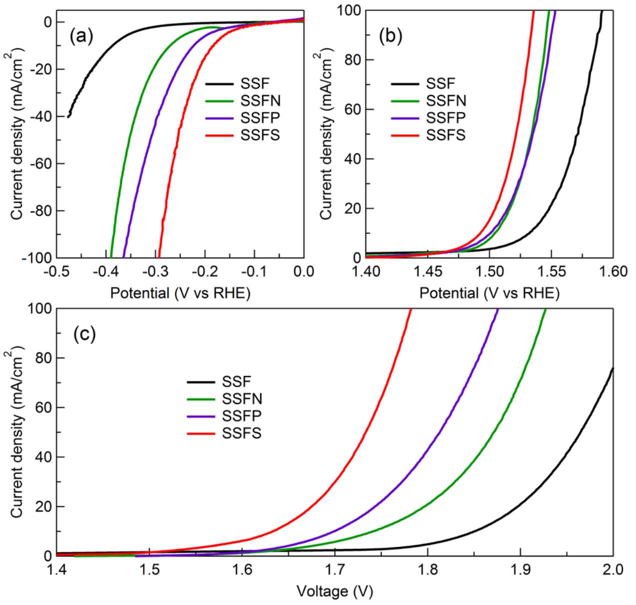

Figure 7. Linear sweep voltammograms of SSF, SSFS, SSFN, and SSFP at a scan rate of 2 mV s^{-1} in 1.0 M KOH (a) for H_2 evolution, (b) for O_2 evolution, and (c) as both cathode and anode catalysts for overall water splitting.

splitting of the four catalyst couples are displayed in Figure 7c, where the activity decreases in the following order: SSFS > SSFP > SSFN > SSF. To produce the benchmark current density of 10 mA cm^{-2}, SSFS, SSFP, SSFN, and SSF required voltages of 1.64, 1.70, 1.73, and 1.85 V, respectively.

■ CONCLUSIONS

In summary, we have demonstrated that facile sulfurization, phosphorization, and nitridation could all substantially boost the electrocatalytic performance of ubiquitous stainless steel for overall water splitting electrolysis. The active species for HER were most likely the surface layers of iron/nickel sulfides, phosphides, and nitrides, whereas OER active composites could be attributed to those in situ-formed iron/nickel (oxy)-hydroxides under electrocatalytic conditions. Synergistically integrating the rich active sites on a surface and highly conductive inner stainless steel skeleton resulted in superior water splitting activity. Given the wide availability, hight level of annual production, and extremely low cost of stainless steel, together with our facile treatment, the surface modification strategy of stainless steel described above represents an effective and versatile method for producing self-supported catalytic systems for various energy-related reactions and paving the way toward the large-scale production of extremely low-cost but competent electrocatalysts.

■ ASSOCIATED CONTENT

Ⓢ Supporting Information

The Supporting Information is available free of charge on the ACS Publications website at DOI: 10.1021/acssuschemeng.7b00182.

Experimental details, figures, and tables (PDF)

■ AUTHOR INFORMATION

Corresponding Author

*E-mail: yujie.sun@usu.edu.

ORCID

Bo You: 0000-0003-1849-0418
Yujie Sun: 0000-0002-4122-6255

Notes

The authors declare no competing financial interest.

■ ACKNOWLEDGMENTS

This work was supported by Utah State University (USU) and the National Science Foundation (CHE-1653978). Y.S. is grateful for the Ralph E. Powe Junior Faculty Enhancement Award (ORAU). We acknowledge the assistance of the Microscopy Core Facility at USU for the SEM and elemental mapping studies.

■ REFERENCES

(1) Gray, H. B. Powering the Planet with Solar Fuel. *Nat. Chem.* **2009**, *1*, 7.

(2) Chu, S.; Majumdar, A. Opportunities and Challenges for a Sustainable Energy Future. *Nature* **2012**, *488*, 294−303.

(3) Jiao, Y.; Zheng, Y.; Jaroniec, M.; Qiao, S. Z. Design of Electrocatalysts for Oxygen- and Hydrogen-Involving Energy Conversion Reactions. *Chem. Soc. Rev.* **2015**, *44*, 2060−2086.

(4) Chen, D. J.; Chen, C.; Baiyee, Z. M.; Shao, Z. P.; Ciucci, F. Nonstoichiometric Oxides as Low-Cost and Highly-Efficient Oxygen Reduction/Evolution Catalysts for Low-Temperature Electrochemical Devices. *Chem. Rev.* **2015**, *115*, 9869−9921.

(5) Zou, X.; Zhang, Y. Noble Metal-Free Hydrogen Evolution Catalysts for Water Splitting. *Chem. Soc. Rev.* **2015**, *44*, 5148−5180.

(6) McCrory, C. C.; Jung, L. S.; Peters, J. C.; Jaramillo, T. F. Benchmarking Heterogeneous Electrocatalysts for the Oxygen Evolution Reaction. *J. Am. Chem. Soc.* **2013**, *135*, 16977−16987.

(7) Wang, H.; Lee, H. W.; Deng, Y.; Lu, Z.; Hsu, P. C.; Liu, Y.; Lin, D.; Cui, Y. Bifunctional Non-Noble Metal Oxide Nanoparticle Electrocatalysts through Lithium-Induced Conversion for Overall Water Splitting. *Nat. Commun.* **2015**, *6*, 7261.

(8) McCrory, C. C.; Jung, L. S.; Ferrer, I. M.; Chatman, S. M.; Peters, J. C.; Jaramillo, T. F. Benchmarking Hydrogen Evolving Reaction and Oxygen Evolving Reaction Electrocatalysts for Solar Water Splitting Devices. *J. Am. Chem. Soc.* **2015**, *137*, 4347−4357.

(9) Jung, S.; McCrory, C. C. L.; Ferrer, I. M.; Peters, J. C.; Jaramillo, T. F. Benchmarking Nanoparticulate Metal Oxide Electrocatalysts for the Alkaline Water Oxidation Reaction. *J. Mater. Chem. A* **2016**, *4*, 3068−3076.

(10) Karunadasa, H. I.; Montalvo, E.; Sun, Y.; Majda, M.; Long, J. R.; Chang, C. J. A Molecular MoS_2 Edge Site Mimic for Catalytic Hydrogen Generation. *Science* **2012**, *335*, 698−702.

(11) Morales-Guio, C. G.; Hu, X. Amorphous Molybdenum Sulfides as Hydrogen Evolution Catalysts. *Acc. Chem. Res.* **2014**, *47*, 2671−2681.

(12) Sun, Y.; Liu, C.; Grauer, D.; Yano, J. J.; Long, R.; Yang, P.; Chang, C. J. Electrodeposited Cobalt-Sulfide Catalyst for Electrochemical and Photoelectrochemical Hydrogen Generation from Water. *J. Am. Chem. Soc.* **2013**, *135*, 17699−17702.

(13) Jiang, N.; Bogoev, L.; Popova, M.; Gul, S.; Yano, J.; Sun, Y. Electrodeposited Nickel-Sulfide Films as Competent Hydrogen Evolution Catalysts in Neutral Water. *J. Mater. Chem. A* **2014**, *2*, 19407−19414.

(14) You, B.; Jiang, N.; Sheng, M.; Sun, Y. Microwave vs Solvothermal Synthesis of Hollow Cobalt Sulfide Nanoprisms for Electrocatalytic Hydrogen Evolution and Supercapacitor. *Chem. Commun.* **2015**, *51*, 4252−4255.

(15) Jiang, N.; Tang, Q.; Sheng, M.; You, B.; Jiang, D. E.; Sun, Y. Nickel Sulfides for Electrocatalytic Hydrogen Evolution Under Alkaline Conditions: A Case Study of Crystalline NiS, NiS_2, And Ni_3S_2 Nanoparticles. *Catal. Sci. Technol.* **2016**, *6*, 1077−1084.

(16) You, B.; Jiang, N.; Sun, Y. Morphology-Activity Correlation in Hydrogen Evolution Catalyzed by Cobalt Sulfides. *Inorg. Chem. Front.* **2016**, *3*, 279−285.

(17) You, B.; Sun, Y. Hierarchically Porous Nickel Sulfide Multifunctional Superstructures. *Adv. Energy Mater.* **2016**, *6*, 1502333.

(18) Chen, W.; Wang, H.; Li, Y.; Liu, Y.; Sun, J.; Lee, S.; Lee, J.-S.; Cui, Y. In Situ Electrochemical Oxidation Tuning of Transition Metal Disulfides to Oxides for Enhanced Water Oxidation. *ACS Cent. Sci.* **2015**, *1*, 244−251.

(19) Stern, L.-A.; Feng, L.; Song, F.; Hu, X. Ni_2P as a Janus Catalyst for Water Splitting: the Oxygen Evolution Activity of Ni_2P Nanoparticles. *Energy Environ. Sci.* **2015**, *8*, 2347−2351.

(20) Ledendecker, M.; Yang, Xi.; Antonietti, M.; Shalom, M. Shalom, M. Disclosing the High Activity of Ceramic Metallics in the Oxygen Evolution Reaction: Nickel Materials as a Case Study. *ChemSusChem* **2016**, *9*, 2928−2932.

(21) Wang, X.; Kolen'ko, Y. V.; Bao, X.-Q.; Kovnir, K.; Liu, L. One-Step Synthesis of Self-Supported Nickel Phosphide Nanosheet Array Cathodes for Efficient Electrocatalytic Hydrogen Generation. *Angew. Chem., Int. Ed.* **2015**, *54*, 8188−8192.

(22) Jiang, N.; You, B.; Sheng, M.; Sun, Y. Electrodeposited Cobalt-Phosphorous-Derived Films as Competent Bifunctional Catalysts for Overall Water Splitting. *Angew. Chem., Int. Ed.* **2015**, *54*, 6251−6254.

(23) You, B.; Jiang, N.; Sheng, M.; Gul, S.; Yano, J.; Sun, Y. High-Performance Overall Water Splitting Electrocatalysts Derived from Cobalt-Based Metal-Organic Frameworks. *Chem. Mater.* **2015**, *27*, 7636−7642.

(24) Jiang, N.; You, B.; Sheng, M.; Sun, Y. Bifunctionality and Mechanism of Electrodeposited Nickel-Phosphorous Films for Efficient Overall Water Splitting. *ChemCatChem* **2016**, *8*, 106−112.

(25) Liu, X.; Dong, J.; You, B.; Sun, Y. Competent Overall Water-Splitting Electrocatalysts Derived from ZIF-67 Grown on Carbon Cloth. *RSC Adv.* **2016**, *6*, 73336−73342.

(26) You, B.; Jiang, N.; Sheng, M.; Bhushan, M. W.; Sun, Y. Hierarchically Porous Urchin-Like Ni_2P Superstructures Supported On Nickel Foam as Efficient Bifunctional Electrocatalysts for Overall Water Splitting. *ACS Catal.* **2016**, *6*, 714−721.

(27) Long, X.; Li, G. X.; Wang, Z. L.; Zhu, H. Y.; Zhang, T.; Xiao, S.; Guo, W. Y.; Yang, S. H. Metallic Iron−Nickel Sulfide Ultrathin Nanosheets as A Highly Active Electrocatalyst for Hydrogen Evolution Reaction in Acidic Media. *J. Am. Chem. Soc.* **2015**, *137*, 11900−11903.

(28) Louie, M. W.; Bell, A. T. An Investigation of Thin-Film Ni-Fe Oxide Catalysts for the Electrochemical Evolution of Oxygen. *J. Am. Chem. Soc.* **2013**, *135*, 12329−12337.

(29) Bates, M. K.; Jia, Q. Y.; Doan, H.; Liang, W. T.; Mukerjee, S. Charge-Transfer Effects in Ni-Fe and Ni-Fe-Co Mixed-Metal Oxides for the Alkaline Oxygen Evolution Reaction. *ACS Catal.* **2016**, *6*, 155−161.

(30) Hou, M.; Lohe, R.; Zhang, J.; Liu, S. H.; Zhuang, X. D.; Feng, X. L. Vertically Oriented Cobalt Selenide/NiFe Layered-Double-Hydroxide Nanosheets Supported on Exfoliated Graphene Foil: An Efficient 3D Electrode for Overall Water Splitting. *Energy Environ. Sci.* **2016**, *9*, 478−483.

(31) Janjua, M. B. I.; Leroy, R. L. Electrocatalyst Performance in Industrial Water Electrolysers. *Int. J. Hydrogen Energy* **1985**, *10*, 11−19.

(32) Moureaux, F.; Stevens, P.; Toussaint, G.; Chatenet, M. Development of An Oxygen-Evolution Electrode from 316L Stainless Steel: Application to The Oxygen Evolution Reaction in Aqueous Lithium−Air Batteries. *J. Power Sources* **2013**, *229*, 123−132.

(33) Yu, F.; Li, F.; Sun, L. Stainless Steel as An Efficient Electrocatalyst for Water Oxidation in Alkaline Solution. *Int. J. Hydrogen Energy* **2016**, *41*, 5230−5233.

(34) Zhong, H.; Wang, J.; Meng, F.; Zhang, X. In Situ Activating Ubiquitous Rust towards Low-Cost, Efficient, Free-Standing, and Recoverable Oxygen Evolution Electrodes. *Angew. Chem., Int. Ed.* **2016**, *55*, 9937−9941.

(35) Schäfer, H.; Beladi-Mousavi, S. M.; Walder, L.; Wollschläger, J.; Kuschel, O.; Ichilmann, S.; Sadaf, S.; Steinhart, M.; Küpper, K.; Schneider, L. L. Surface Oxidation of Stainless Steel: Oxygen Evolution Electrocatalysts with High Catalytic Activity. *ACS Catal.* **2015**, *5*, 2671−2680.

(36) Schäfer, H.; Sadaf, S.; Walder, L.; Kuepper, K.; Dinklage, S.; Wollschläger, J.; Schneider, L. L.; Steinhart, M.; Hardege, J.; Daum, D. Stainless Steel Made to Rust: A Robust Water-Splitting Catalyst with Benchmark Characteristics. *Energy Environ. Sci.* **2015**, *8*, 2685−2697.

(37) Schäfer, H.; Küpper, K.; Wollschläger, J.; Kashaev, N.; Hardege, J.; Walder, L.; Mohsen Beladi-Mousavi, S.; Hartmann-Azanza, B.; Steinhart, M.; Sadaf, S.; Dorn, F. Oxidized Mild Steel S235: An Efficient Anode for Electrocatalytically Initiated Water Splitting. *ChemSusChem* **2015**, *8*, 3099−3110.

(38) Schäfer, H.; Chevrier, D. M.; Kuepper, K.; Zhang, P.; Wollschlaeger, J.; Daum, D.; Steinhart, M.; Heß, C.; Krupp, U.; Müller-Buschbaum, K.; Stangl, J.; Schmidt, M. X20CoCrWMo10−9//Co_3O_4: A Metal−Ceramic Composite with Unique Efficiency Values for Water-Splitting in The Neutral Regime. *Energy Environ. Sci.* **2016**, *9*, 2609−2622.

(39) Schäfer, H.; Chevrier, D. M.; Zhang, P.; Stangl, J.; Müller-Buschbaum, K.; Hardege, J. D.; Kuepper, K.; Wollschläger, J.; Krupp, U.; Dühnen, S.; Steinhart, M.; Walder, L.; Sadaf, S.; Schmidt, M. Electro-Oxidation of Ni42 Steel: A Highly Active Bifunctional Electrocatalyst. *Adv. Funct. Mater.* **2016**, *26*, 6402−6417.

(40) Yang, F. C.; Guo, Z. G. A Facile Approach to Transform Stainless Steel Mesh into pH-Responsive Smart Material. *RSC Adv.* **2015**, *5*, 13635−13642.

(41) Putatunda, S. K. Corrosion Behavior of Sensitized Austenitic (AISI 304) Stainless Steel in A Sulfidizing Atmosphere. *Mater. Sci. Eng.* **1986**, *82*, L7−L11.

(42) Kai, W.; Leu, C. T.; Lee, P. Y. Effects of Sulfur Pressure on The Sulfidation Behavior of 310 Stainless Steel. *Oxid. Met.* **1996**, *46*, 185−211.

(43) Lu, X. Y.; Zhao, C. Electrodeposition of Hierarchically Structured Three-Dimensional Nickel-Iron Electrodes for Efficient Oxygen Evolution at High Current Densities. *Nat. Commun.* **2015**, *6*, 6616.

(44) Biesinger, M. C.; Payne, B. P.; Grosvenor, A. P.; Lau, L. W. M.; Gerson, A. R.; Smart, R. C. Resolving Surface Chemical States in XPS Analysis of First Row Transition Metals, Oxides and Hydroxides: Cr, Mn, Fe, Co and Ni. *Appl. Surf. Sci.* **2011**, *257*, 2717−2730.

(45) Hong, W. T.; Risch, M.; Stoerzinger, K. A.; Grimaud, A.; Suntivich, J.; Yang, S. H. Toward The Rational Design of Non-Precious Transition Metal Oxides for Oxygen Electrocatalysis. *Energy Environ. Sci.* **2015**, *8*, 1404−1427.

(46) Merrill, M. D.; Dougherty, R. C. Metal Oxide Catalysts for the Evolution of O_2 from H_2O. *J. Phys. Chem. C* **2008**, *112*, 3655−3666.

(47) Ho, J. C. K.; Piron, D. L. Active Surface Area in Oxide Electrodes by Overpotential Deposited Oxygen Species for The Oxygen Evolution Reaction. *J. Appl. Electrochem.* **1996**, *26*, 515−521.

(48) Subbaraman, R.; Tripkovic, D.; Strmcnik, D.; Chang, K.-C.; Uchimura, M. A.; Paulikas, P.; Stamenkovic, V.; Markovic, N. M. Enhancing Hydrogen Evolution Activity in Water Splitting by Tailoring Li^+-$Ni(OH)_2$-Pt Interfaces. *Science* **2011**, *334*, 1256−1260.

(49) Nichols, E. M.; Gallagher, J. J.; Liu, C.; Su, Y.; Resasco, J.; Yu, Y.; Sun, Y.; Yang, P.; Chang, M. C. Y.; Chang, C. J. Hybrid Bioinorganic Approach to Solar-to-Chemical Conversion. *Proc. Natl. Acad. Sci. U. S. A.* **2015**, *112*, 11461−11466.

(50) Liu, C.; Colón, B. C.; Ziesack, M.; Silver, P. A.; Nocera, D. G. Water Splitting−Biosynthetic System with CO_2 Reduction Efficiencies Exceeding Photosynthesis. *Science* **2016**, *352*, 1210−1213.

(51) Ledendecker, M.; Schlott, H.; Antonietti, M.; Meyer, B.; Shalom, M. Experimental and Theoretical Assessment of Ni-Based Binary Compounds for the Hydrogen Evolution Reaction. *Adv. Energy Mater.* **2017**, *7*, 1601735.